Hard X-ray Detector (HXD) on Board Suzaku

Tadayuki Takahashi[1,2], Keiichi Abe[3], Manabu Endo[4], Yasuhiko Endo[3*],
Yuuichiro Ezoe[1], Yasushi Fukazawa[5], Masahito Hamaya[6] Shinya Hirakuri[2†],
Soojing Hong[3,7‡], Michihiro Horii[6], Hokuto Inoue[1,2§], Naoki Isobe[7], Takeshi Itoh[2],
Naoko Iyomoto[2] ¶ Tuneyoshi Kamae[8], Daisuke Kasama[2‖] Jun Kataoka[1,2**]
Hiroshi Kato[7], Madoka Kawaharada[2], Naomi Kawano[5] Kengo Kawashima[5],
Satoshi Kawasoe[5], Tetsuichi Kishishita[1,2], Takao Kitaguchi[2], Yoshihito Kobayashi[1,2††],
Motohide Kokubun[2], Jun'ichi Kotoku[2**], Manabu Kouda[1,2 ‡‡], Aya Kubota[7],
Yoshikatsu Kuroda[4], Greg Madejski[8], Kazuo Makishima[2,7], Kazunori Masukawa[4],
Yukari Matsumoto[2†] Takefumi Mitani[1,2], Ryohei Miyawaki[2], Tsunefumi Mizuno[5],
Kunishiro Mori[9], Masanori Mori[3,7§§], Mio Murashima[2¶¶], Toshio Murakami[10],
Kazuhiro Nakazawa[1], Hisako Niko[2], Masaharu Nomachi[11], Yuu Okada[2†],
Masanori Ohno[5], Kousuke Oonuki[1,2], Naomi Ota[7], Hideki Ozawa[11],
Goro Sato[1,2] ¶, Shingo Shinoda[12], Masahiko Sugiho[2‖] Masaya Suzuki[2***],
Koji Taguchi[6], Hiromitsu Takahashi[5], Isao Takahashi[2†††]
Shin'ichiro Takeda[1,2], Ken-ichi Tamura[1], Takayuki Tamura[1,2],
Takaaki Tanaka[1,2], Chiharu Tanihata[1,2], Makoto Tashiro[3],
Yukikatsu Terada[7], Shin'ya Tominaga[5], Yasunobu Uchiyama[1,2], Shin Watanabe[1,2],
Kazutaka Yamaoka[13], Takayuki Yanagida[2], and Daisuke Yonetoku[10],

[1]*Department of High Energy Astrophysics, Institute of Space and Astronautical Science (ISAS),*
Japan Aerospace Exploration Agency (JAXA), 3-1-1 Yoshinodai, Sagamihara, 229-8510
takahasi@astro.isas.jaxa.jp
[2]*Department of Physics, Graduate School of Science, University of Tokyo, Hongo 7-3-1, Bunkyo, 113-0033*
[3]*Department of Physics, Saitama University, 255 Shimo-Okubo, Sakura, Saitama, 338-8570*
[4]*Mitsubishi Heavy Industry, Co., Ltd., Nagoya Guidance and Propulsion Systems Works,*
1200 Higashi Tanaka, Komaki, 485-8561
[5]*Department of Physical Science, Hiroshima University, 1-3-1 Kagamiyama, Higashi-Hiroshima, 739-8526*
[6]*Meisei Electric, Co., Ltd., 2223 Naganuma-cho, Isezaki, 372-8585*
[7]*The Institute of Physical and Chemical Research (RIKEN), 2-1 Hirosawa, Wako, 351-0198*
[8]*Stanford Linear Accelerator Center (SLAC), 2575 Sand Hill Road, Menlo Park, CA 94025, USA.*
[9]*Clear Pulse, Co., Ltd., 6-25-17 Chuuou, Ota, 143-0024*
[10]*Department of Physics, Kanazawa University, Kakuma-machi, Kanazawa, 920-1192*
[11]*Department of Physics, Osaka University, 1-1 Machikaneyama, Toyonaka, 560-0043*
[12]*SSD Corp., 3-34-13-301 Togashira, Toride, 302-0034*
[13]*Department of Physics and Mathematics Aoyama Gakuin University,*
5-10-1 Fuchinobe, Sagmihara, 229-8558

Abstract

The Hard X-ray Detector (HXD) on board Suzaku covers a wide energy range from 10 keV to 600 keV by combination of silicon PIN diodes and GSO scintillators. The HXD is designed to achieve an extremely low in-orbit background based on a combination of new techniques, including the concept of well-type active shield counter. With an effective area of 142 cm^2 at 20 keV and 273 cm^2 at 150 keV, the background level at the sea level reached $\sim 1\times10^{-5}$ cts s^{-1} cm^{-2} keV^{-1} at 30 keV for the PIN diodes, and $\sim 2\times10^{-5}$ cts s^{-1} cm^{-2} keV^{-1} at 100 keV, and $\sim 7\times10^{-6}$ cts s^{-1} cm^{-2} keV^{-1} at 200 keV for the phoswich counter. Tight active shielding of the HXD results in a large array of guard counters surrounding the main detector parts. These anti-coincidence counters, made of $\sim$4 cm thick BGO crystals, have a large effective area for sub-MeV to MeV γ-rays. They work as an excellent γ-ray burst monitor with limited angular resolution ($\sim 5°$). The on-board signal-processing system and the data transmitted to the ground are also described.

1. Introduction

Suzaku is the fifth in a series of Japanese X-ray astronomy satellite with important US instrument contributions(Mitsuda et al. 2006). Its scientific payload consists of two kinds of co-aligned instruments, the X–ray Imaging Spectrometers (XIS) (Koyama et al. 2006) and the Hard X–ray Detector (HXD). The HXD extends the bandpass of the observatory to much higher energies with its 10-600 keV bandpass. While the bandpass of previous Japanese X-ray satellites was primarily below $\sim$20 keV, where thermal emission predominates, the energy range of 10 - several 100 keV is where the radiation from the high-energy celestial sources is mainly non-thermal. There were several missions that covered this energy range, but sensitive observations were very difficult, since the signal from X-ray sources is much weaker than the detector background, and also because the fluctuations of such background are large at orbital environments in inclined low Earth orbits.

The main challenge of hard X-ray to gamma-ray spectroscopy is that the signal intensity from the source is usually weaker than detector background. The main causes of the background include diffuse gamma rays, emission from radioactive nuclei due to activation of the detector, itself, and also cosmic rays such as protons and other heavy ions. Besides, Compton down-scattering, dominant at higher energies, makes a proper X-ray event appear as background at a lower energy. Based on the experience accumulated through a series of balloon experiments (Kamae et al. 1992; Takahashi et al. 1993), the HXD is designed to minimize the background level by utilizing two concepts: "Well-type active shield" and "Compound-eye configuration"

and hence to achieve a higher sensitivity than any previous instrument in the energy range between 10 keV and several 100 keV.

Since Suzaku is the recovery mission to the original *Astro-E*, which was lost in the launch accident in 2000, its basic design is the same as that of *Astro-E*. We have designed and developed the HXD basically in the same manner as the previous HXD on board the lost *Astro-E* (Kamae et al. 1996; Tashiro et al. 2002). However, we employed a limited range of improvements, particularly concerning the sensor and analog electronics. The HXD fabrication was carried out involving detailed qualification at every step, with a special emphasis on the verification of the newly introduced improvements. This paper describes the design of the HXD system and its ground performance. An accompanying paper (Kokubun et al. 2006; hereafter Paper II) considers the in-orbit performance of the HXD. Early reports on the HXD system and ground calibration can be found in previous publications (Kokubun et al. 2004; Kawaharada et al. 2004; Terada et al. 2005; Fukazawa et al. 2006; Yamaoka et al. 2006 and references therein.)

Fig. 1. Hard X–ray Detector before installation.

2. The HXD System

The HXD is a non-imaging and collimated instrument. The system is composed of the sensor part (HXD sensor or HXD-S), an analog electronic system (HXD-AE), and a digital electronics system (HXD-DE). A photograph of HXD-S is shown in figure 1. As described in
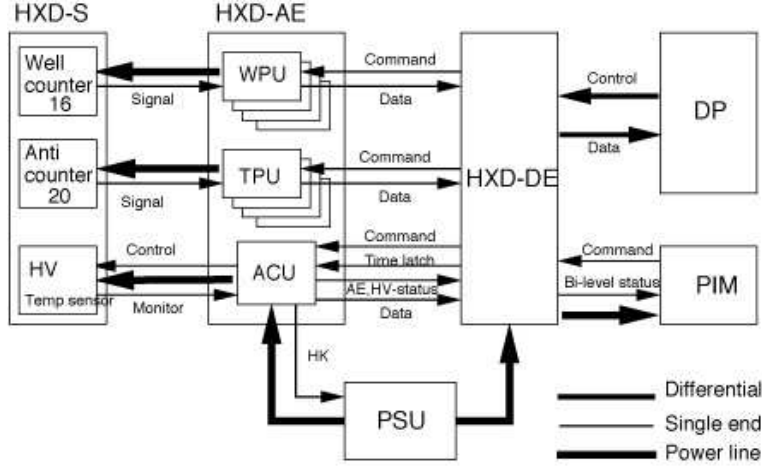
Fig. 2. Block diagram of the HXD system and signal flow between components.

Table 1. Characteristics of the HXD system on board Suzaku

HXD	Field of View	$4.5° \times 4.5°$ ($\gtrsim 100$ keV)
	Field of View	$34' \times 34'$ ($\lesssim 100$ keV)
	Bandpass	$10 - 600$ keV
	– PIN	$10 - 70$ keV
	– GSO	$40 - 600$ keV
	Energy Resolution (PIN)	~ 3.0 keV (FWHM)
	Energy Resolution (GSO)	$7.6/\sqrt{E_{MeV}}$ % (FWHM)
	Effective area	$\sim 160\,\mathrm{cm}^2$ at 20 keV, $\sim 260\,\mathrm{cm}^2$ at 100 keV
	Time Resolution	61 μs or 31 μs
HXD-WAM[a]	Field of View	2π (non-pointing)
	Bandpass	50 keV – 5 MeV
	Effective Area	800 cm^2 at 100 keV / 400 cm^2 at 1 MeV
	Time Resolution	15.625 ms or 31.25 ms for GRB, 1 s for All-Sky-Monitor

a: Shield counters of the HXD sensor part act as a wide-band all-sky monitor (WAM).

the block diagram (figure 2), HXD-AE receives analog signals from HXD-S, selects the proper events and sends their digitized data to HXD-DE. HXD-DE then formats the data packets to send them to the ground via the satellite data processor (DP). Commands to the HXD are received by the peripheral interface module (PIM) from the satellite data handling unit, and transmitted to HXD-DE. All power is supplied from a power-supply unit called HXD-PSU. The operating temperature of HXD-S is designed to be -20ºC. The characteristics of the HXD are summarized in table 1.

Fig. 3. Schematic drawing of HXD-S. It consists of 16 well-counter units and 20 anti-counter units.

3.   HXD Sensor (HXD-S)

Since the background level sets the sensitivity limit in the hard X-ray band, the HXD is designed to minimize the background by its improved phoswich (acronym for PHOSphor sandWICH) configuration for the energy region above 40 keV and the adoption of newly-developed thick silicon PIN diodes for the energies below ~ 70 keV. Our detector ensures a low background though the following techniques.

1. Well-type active shield:
   In phoswich counters, two crystals with different decay times are used for the detection part (faster decay time) and the shielding part (slower decay time), and both signals are extracted by a single photomultiplier. The improvement is that the shield is shaped in a well, so that it also acts as an active collimator (well-type active shield). This narrows the

5

Configuration of sensor units (Top view)

T00	T01	T02	T03	T04	T10
T34	W00	W01	W10	W11	T11
T33	W03	W02	W13	W12	T12
T32	W30	W31	W20	W21	T13
T31	W33	W32	W23	W22	T14
T30	T24	T23	T22	T21	T20

Y ↑ → X

P0	P1
P3	P2

PIN in Well 1 unit
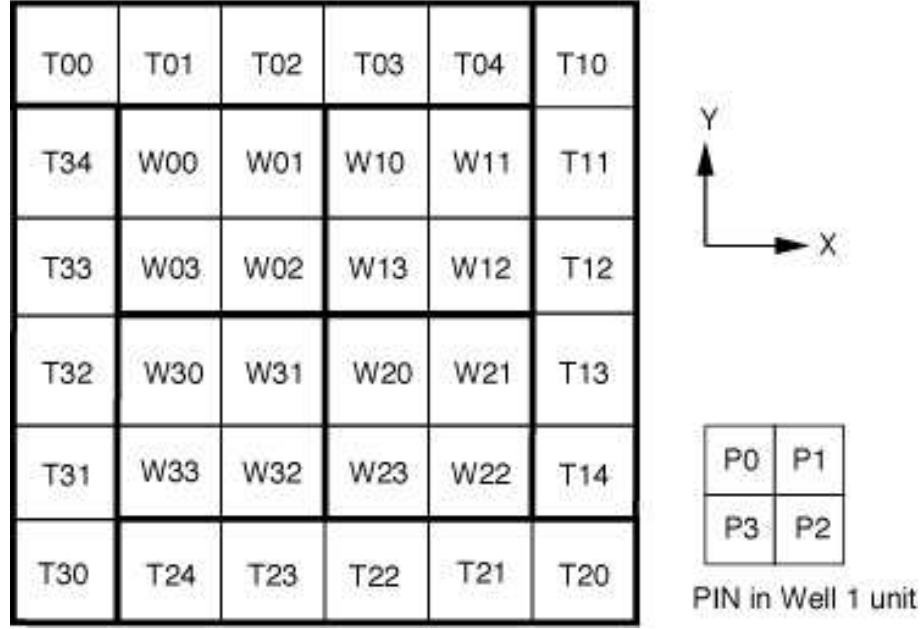
Fig. 4. Numbering of the well and anti counter units when HXD-S is viewed from the top. There are 16 well-counter units from W00 to W33 and 20 anti-counter units from T00 to T34. Y direction corresponds to the direction toward Sun when the HXD is mounted to the satellite.

   field of view (FOV) of the phoswich counter without any additional passive material, and results in the main detection part having an active shield of almost 4π of its surrounding (well-type phoswich counter). In the HXD, the well-type shield provides very efficient shielding for the the PIN diode, which is read out independently.

2. Compound eye configuration:
   HXD is modular, that is, consisting of a number of units. Each well-type phoswich counter unit has a simple shape and operates at a modest count rate by itself. In the HXD, we increase the photon collecting area by placing individual units in a matrix. In this configuration, each unit also becomes an active shield for adjacent units (compound eye configuration). It is also useful to reduce the possible dead time if parallel processing of each unit could be implemented. For additional shielding ofr the outer most units, thick anti-coincidence counters are placed surrounding the well units.

   The main detection part of the phoswich counter in HXD-S is a Gadolinium silicate crystal (GSO; $Gd_2SiO_5(Ce)$) buried deep in the bottom of a well-shape bismuth germanate crystal (BGO; $Bi_4Ge_3O_{12}$) (hereafter we refer it as well-counter unit). As shown in the schematic drawing (figure 3), the HXD-S consists of 16 phoswich counters with 4 silicon PIN diodes in each, and 20 surrounding BGO anti-coincidence shield counters (anti-counter unit). All of the 16 well-counter units and 20 anti-counter units work independently. The numbering of the

well-counters and anti-counters, which is frequently referred to in various technical documents, is shown in figure 4

During operation of the HXD, instead of rocking observation, we plan to perform background subtraction by modeling the background spectrum, as was done in the LAC detector in Ginga satellite (Hayashida et al. 1989). Thus the sensitivity will depend on the accuracy of the background modeling. If the background flux can be kept low, any systematic error of the modeling will have little effect on the spectrum of sources with a given flux. Since radioactive contamination in the detection part contributes to the background directly, special care was taken to select materials for the components used in the HXD sensor.

3.1. Well-counter units

In the HXD, each well-counter unit consists of five components (figure 5) crystals, PIN diodes, fine collimators, a photomultiplier, and front-end electronics. The mass of each unit is 4.63 kg. The crystals in the well-counter unit are four 5 mm-thick GSO scintillators with dimensions of 24 mm $\times$ 24 mm, and BGO scintillators for active shields. A photomultiplier, HAMAMATSU R6231-07, is attached to the counter unit to collect scintillation light from both GSO and BGO scintillators. The dynode signal from the photomultiplier is first processed by the preamplifier mounted in the housing of HXD-S, In the well-counter unit, the BGO scintillator is further divided into two pieces; a block-like section called "BGO bottom piece", and a well-shaped long section called "BGO top piece". The BGO top piece is not a simple "well", but has cross-shaped inner BGO plates of 3 mm thickness to divide the "well" into four narrow collimators. The four GSOs are placed on the BGO bottom piece and surrounded by four long square tubes of the BGO top piece. The BGO top piece actively restricts the field of view to 4°.6 $\times$ 4°.6. By thus collimating the field of view, and rejecting those events that deposit all, or part, of energy in BGO, the well-Counter unit attains high sensitivity.

In addition to their large stopping power, the reason for having two different types of crystals for the sensors and the shields is their very different rise/decay times: of ~ 706 ns for BGO, and ~ 122 ns for GSO, at a working temperature of -20°C (Kamae et al. 1992). This allows an easy discrimination of the sensor signal from the shield signals, where a single photomultiplier can discriminate between the two types of scintillators in which an event may have occurred. Any particle events or Compton events that are registered by both the BGO and GSO can be rejected by this phoswich technique. The GSO/BGO phoswich has several advantages over more conventional (e.g., NaI/CsI) combinations. Firstly, both GSO and BGO features a higher stopping power for γ-rays. Secondly, they have fast decay times suitable for a fast signal processing, and a large difference in the decay times between the two components, which makes pulse-shape discrimination easier. Furthermore, the number of long-lived γ-rays due to activations caused by charged particles irradiating the detector is smaller, compared with other high-light-yield scintillation materials such as YAP and NaI(Tl), if we normalize

7

by the absorption thickness in the hard X-ray energy range. In table 2, we summarize the properties of the GSO and the BGO scintillators, together with those of NaI and CsI for a reference. In the HXD, we use a GSO crystal made by Hitachi Chemical [1] with highly purified materials supplied by Shin-etsu Chemical Co Ltd. [2] in order to reduce any possible intrinsic background in the material. This purification is found to be very effective to increase the light output of the GSO scintillator (Kamae et al. 2002)
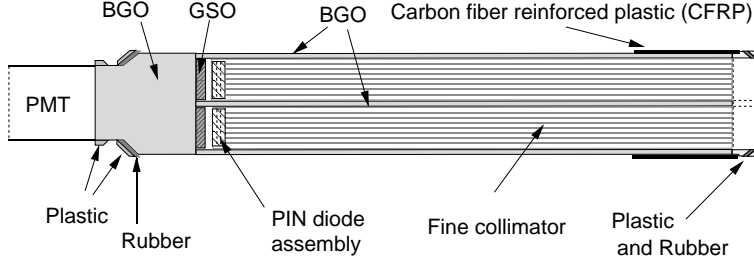

Fig. 5. A schematic drawing of the well-counter unit. The silicon PIN diode with dimensions of 21.5 mm $\times$ 21.5 mm $\times$ 2 mm is placed in the deep well just above the GSO scintillator. The 24 mm $\times$ 24 mm GSO scintillator with a thickness of 5 mm is glued to the bottom part of the well-type BGO shield.

Table 2. Properties of the GSO and BGO scintillators, together with those of NaI(Tl) and CsI(Tl) scintillators.

	GSO(Ce)	BGO	NaI(Tl)	CsI(Tl)
	$Gd_2SiO_5(Ce)$	$Bi_4Ge_3O_{12}$	NaI	CsI
Effective decay time (ns)@20°C	86	353	230	1000
Effective decay time (ns)@−20°C	122	706		
Effective atomic number	59	74	50	54
Density (g/cm^3)	6.7	7.1	3.7	4.5
Radiation length (cm)	1.4	1.2	2.6	1.9
Peak emission (nm)	430	480	410	565
Light yield (photons/MeV)*	~ 10000	~ 4000	38000	32000
Index of refraction (at λ_{em})	1.9	2.15	1.85	1.80
Hygroscopicity	none	none	yes	little

* Light yield measured with a bi-alkali photomultiplier.

Since the GSO part covers an energy range of $\sim$ 40–600 keV, another detector element is needed to assure coverage over the energy range down to that of the XIS (< 12 keV). The low energy response of the HXD is provided by 2 mm thick PIN silicon diodes, each placed in front of a GSO crystal to form a PIN-GSO pair as the detection part of the well-counter unit. The diodes absorb X–rays with energies below $\sim$ 70 keV, but gradually become transparent to

[1] http://www.hitachi-chem.co.jp/english/index.html

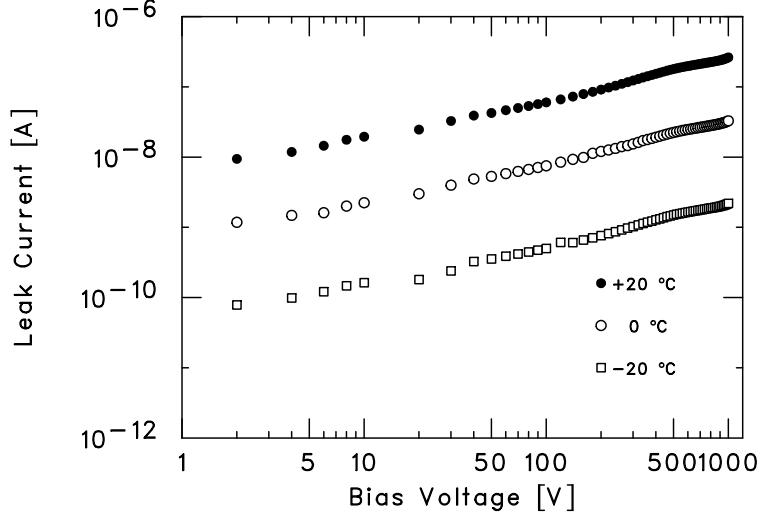[2] http://www.shinetsu.co.jp/e/index.shtml

Fig. 6. Typical leakage current of a 2 mm-thick silicon PIN diode developed for the HXD as a function of the bias voltage. Data obtained at three different temperatures are shown.

harder X–rays, which in turn, reach and are registered by, the GSO detectors. Such PIN diodes were specially developed jointly with Hamamatsu Photonics K.K. [3] to have 2 mm thickness (Ota et al. 1999). These thick PIN diodes were manufactured from highly purified silicon wafers, and can be fully depleted at a bias voltage of ~ 500 V due to their high resistivity (20–30 kΩ cm). In order to lower the leakage current and attain stable operation, specially designed guard rings are built in the PIN diodes. The geometrical area of the PIN diode, including the guard ring, is 21.5 mm $\times$ 21.5 mm. Figure 6 show current-voltages curves obtained from a typical PIN diode taken at -20°C, 0°C and 20°C. The PIN diodes in the HXD have a leakage current of less than 2.2 nA at 500 V and@ -20°C, and do not show any breakdown even under the bias voltage of 1000 V. In order to minimize the background gamma-ray contamination for the PIN, we selected low-background materiasl for the cables and the package. The adoption of a ceramic with a purity higher than 96 % for the PIN package was required to avoid any continuum gamma-ray background due to β-decay electrons from potassium in the material.

In the energy range of the PIN diode, the dominant background component is the cosmic X-ray background. Therefore, having a narrow FOV is the most effective method to reduce the background contamination. For this purpose, passive shields called "fine collimators" are inserted in the BGO well-type collimator above the PIN diodes. The fine collimator is made of 50 μm thick phosphor bronze sheets arranged to form a square array of 8 $\times$ 8 square channels each of 3 mm width and 300 mm length. Both the BGO collimator and the fine collimator define the FOV of the well-counter unit. Because of the finite thickness, the FOV changes with the photon energy. Below ~ 100 keV, the passive fine collimators define a $34' \times 34'$ full-width half-maximum (FWHM) square FOV. Above ~ 100 keV, the fine collimators become transparent
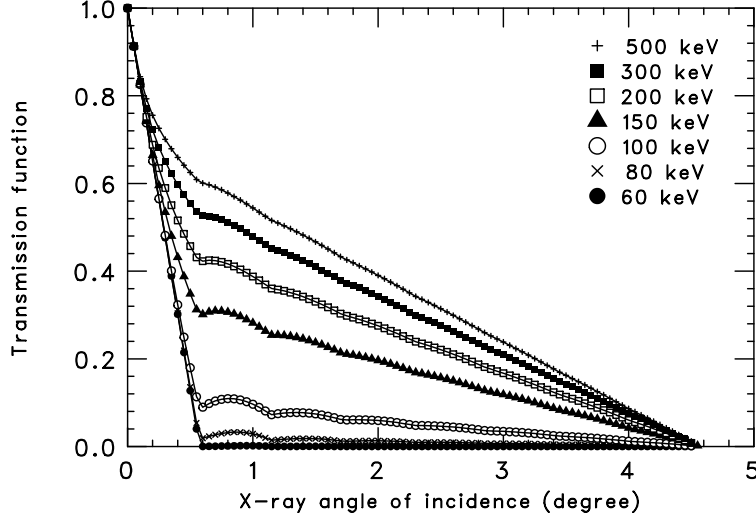

Fig. 7. Angular transmission function of the fine collimator calculated at an azimuth angle of 0 degree. The 0 degree azimuth angle is defined along the positive x-axis in figure 4
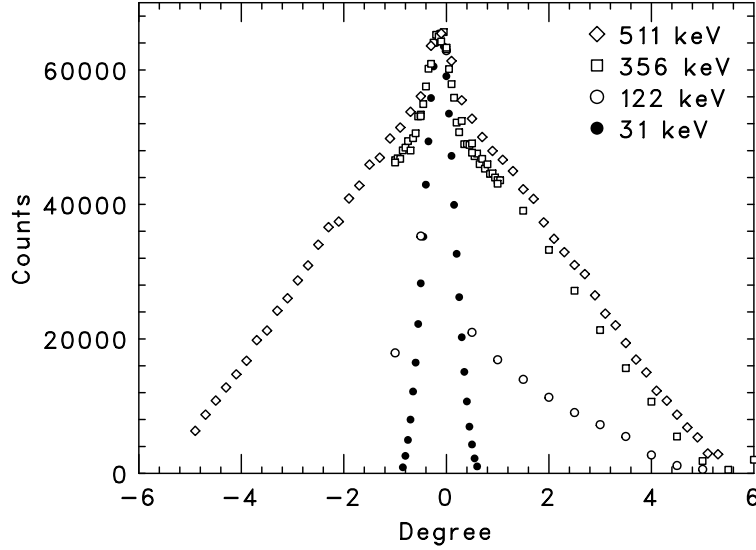

Fig. 8. Angular responses of well-counter unit, measured with radio isotope sources (511 keV from ^{22}Na, 356 keV from ^{133}Ba, 122 keV from ^{152}Eu, 31 keV from ^{133}Ba) placed 280 cm away. The response is consistent with the calculation when the finite distance from the sources to the unit is taken into account.

and the BGO active collimator defines a 4.5°× 4.5 ° FWHM square opening. Figure 7 shows the calculation of the energy dependence of the angular response. The collimator becomes transparent above ∼ 100 keV, approaching the larger FOV of 4.5° × 4.5° (FWHM), defined by the BGO well. The angular response measured with γ-ray lines from radio isotope sources located at limited distance is consistent with the calculation (figure 8).

A Well-counter unit is completed by assembling all of the above and several additional components, and further incorporating several additional attachments. In order to attain a

10
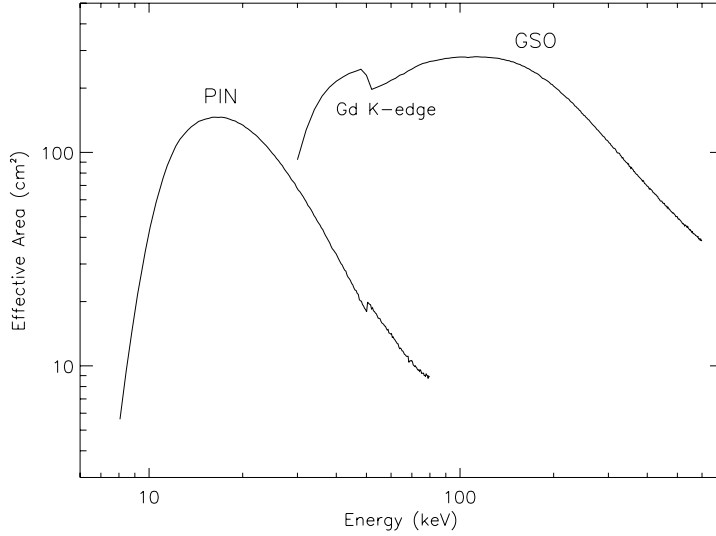
Fig. 9. Total effective area of the HXD detectors, PIN and GSO, as a function of energy. Photon absorption by materials in front of the device is taken into account.

high light-collection efficiency through the better light reflection at the surface, we painted the BGO pieces with $BaSO_4$ and wrapped them with a Gore-Tex sheet. Similarly, the top and side surfaces of each GSO was wrapped by Gore-Tex sheets for better light reflection. The mechanical support structures at the top and bottom protect each well-counter unit from any vibration and shock during the launch. The structures are made of visco-elastic rubber, plastic adapters, and carbon fiber reinforced plastics (CFRP) plates. A detailed description of the construction of the units is provided in Nakazawa et al. (1999). Figure 9 shows the effective area of 16 Well-counter units, which was based on the photo-peak efficiency calculated by Monte Carlo simulations using the EGS4 code (Nelson et al. 1985). The total geometrical area of the PIN diodes is 160 cm^2, while that of the GSO crystals is 350 cm^2. It is clear that the overlapping energy region between GSO and PIN, $\sim$ 40–70 keV, is well covered.

3.2. Anti-counter units

For additional shielding of the outermost well-counter units, 20 anti-counter units, each made of thick (average 2.6 cm) BGO pillars, surround a well-counter matrix. This reduces the cosmic proton flux on the PINs and the GSOs by an order of magnitude. It also serves to reduce Compton scattered events as well as nuclear activation background events. Each unit is viewed by a photomultiplier (HAMAMATSU R3998-01). The prime function of the anti-counter units is to provide hit-pattern information to the Well-counter units. The anti-counter units have a wedge-like structure for saving their mass while obtaining the same path length of the BGO

11

scintillator viewed from the PIN and the GSO in the well-counter units. The mass of each unit is 4.12 kg for 16 units except for the corner units with a mass of 2.72 kg. The geometrical area of the anti-counter wall is as large as ~ 800 cm^2 per side, and its effective area is ~ 400 cm^2 even for 1 MeV γ-rays. Therefore, they are also utilized as an excellent γ-ray burst detector in the energy range between 50 keV and 5 MeV. According to a MonteCarlo simulation, if a gamma-ray burst occurs with an intensity of 1 cnts/s/cm^2 in $50-300$ keV, the spectrum with parameters of $\alpha = -1.0, \beta = -2.3$ and $E_0 = 250$ keV in the Band function (Band et al. 1993), and a duration of 20 sec, is captured by two side faces of the anti-counter units, we can determine its one dimensional position with an accuracy of $\sim 5°$, by comparing signal counts from the four sides. As shown in figure 10, the anti-counter units have the largest effective area compared with other current or future γ-ray burst (GRB) detectors, including the GLAST/GBM and the Swift/BAT in the MeV range. Above 300 keV, the HXD has the largest effective area. The detailed description of the WAM and its in-flight performance is described in Yamaoka et al. (2006).
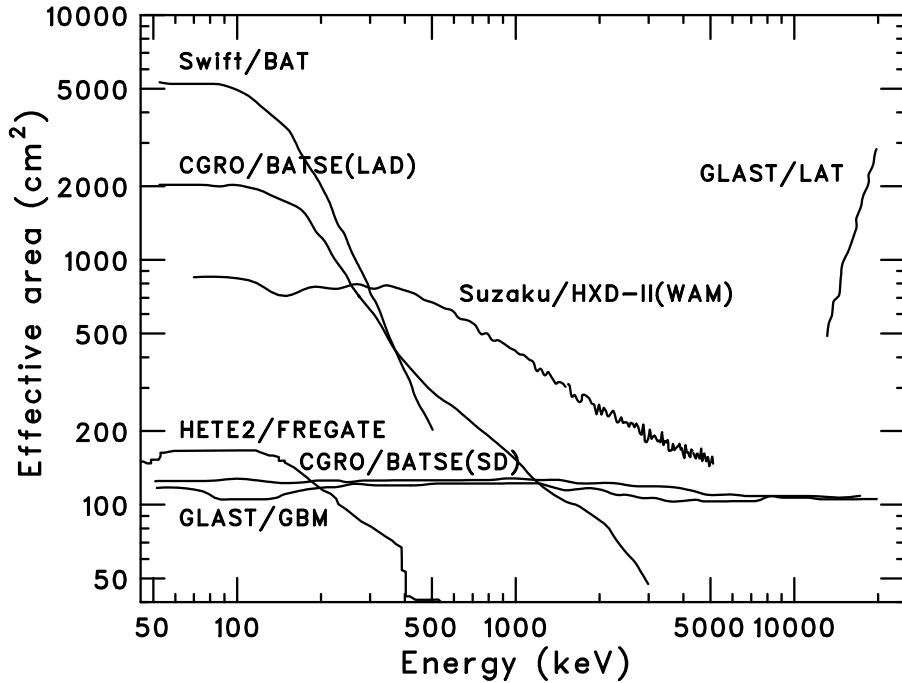
Fig. 10. Comparison of the effective area of the anti-counter units per side (excluding the "Corner Units") and those of other GRB detectors.

3.3. HXD Housing

The housing structure for HXD-S is designed to hold 36 detector units in HXD-S. The function of the housing is to protect the units mechanically, to minimize any temperature gradient among the units, and to reduce electrical noise. These requirements should be realized within the limited space and mass allowed to the instrument. For this purpose, CFRP and

Magnesium alloy are adopted for the material to be used.

The HXD-S housing is made of three components: the top lid and the center body part made of CFRP, and the bottom structure made of Magnesium-alloy. CFRP is selected not only for its strength and light mass; it also has a lower thermal expansion compared with the BGO crystal, and will not give any stress to the detectors once HXD-S is cooled to the operating temperature of -20°C in orbit. The top lid has 64 square openings matching the FOV of the well units; another thin (400μm) plate of CFRP is used to cover them for optical light blocking. The total mass of the housing is 27.3 kg.

To achieve an operating temperature of $-20\pm5^{\circ}$C, HXD-S is thermally decoupled from environment by multi-layer insulator (MLI), and mounted on a cold-plate, which is attached to the lower deck of the spacecraft. The cold-plate is kept at low temperature via radiation cooling, and is also equipped with a heater to control its temperature. The heat generated in the sensor part is ~ 17 W, half of which is from the high voltage (HV) units that are attached to the bottom structure of the housing. Therefore the HV units are placed outside of the MLI, thermally insulated from the main body of the sensor, and radiatively coupled to the spacecraft. The remaining power is dissipated in the pre-amplifiers and PMT bleeders. Except for the locations of the HV units and other heat sources, HXD-S is designed to achieve a rather uniform temperature within a few degree. The thermal design of HXD-S was verified in a thermal-vacuum test using the spacecraft thermal model. Further details on the mechanical structure are described in Nakazawa et al. (1999).

4.   Onboard Data Processing System

The electronic system of the HXD plays a crucial role in obtaining the best performance of the instrument. The total number of signal channels extracted from HXD-S to be processed is 116 (96 channels for the well units and 20 channels for the anti-counter units). A robust and stable electronic system is required to process data from these channels under nominal constraints for a space experiment, including in particular a severe power limitation. Furthermore, the real time performance of the system is critical to minimize the dead time caused by triggers issued randomly from these channels. The onboard data processing system of the HXD is thus carefully designed (Takahashi et al. 1998; Tanihata et al. 1999), incorporating two major system components, namely an analog processing system, called HXD-AE (analog electronics), and a CPU-based processing system, called HXD-DE (figure 2). Here we briefly describe HXD-AE, HXD-DE, and the output data.

4.1.   Analog Electronics (HXD-AE)

HXD-AE consists of one control board called Analog Control Unit (ACU) and eight signal processing boards. The latter is broken into two types, four well processing unit (WPU) boards for the Well counter units, and four transient processing unit (TPU) boards for the anti-
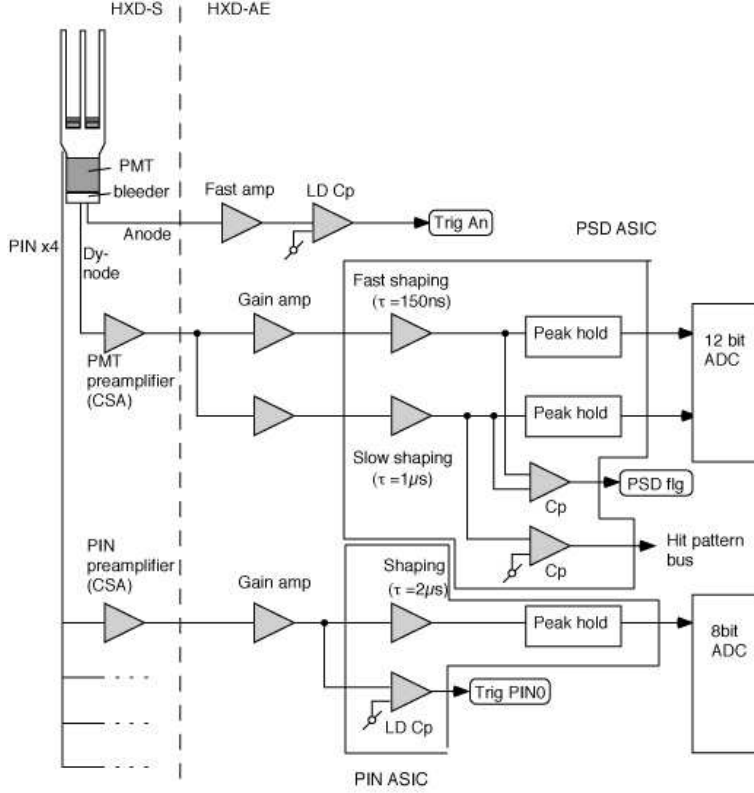
Fig. 11. Signal flow from a well counter unit to a WPU board. A pair of anode and dynode signals from the bleeder and four PIN diode signals are processed in one block. A WPU contains four of these blocks, and handles signals from four well-counter units.

counter units. While the well counter units acquire data from target sources, the anti-counter units have an additional function of monitoring transient sources (including gamma-ray bursts), in addition to its basic role as active shields.The ACU is provided power from HXD-PSU, and controls the power lines to the other electronic boards in HXD-AE as well as those to HXD-S. It also handles house keeping (HK) data, such as high voltage values and temperatures of the scintillators and photomultiplier tubes.

Each WPU and TPU, respectively, handles four well units and five anti-counter units. All WPU/TPU and ACU boards are connected to the backplane of the AE housing. In order to reject the Compton events that occur in the compound eye configuration of the HXD, it is important for each unit to be informed of the presence or absence of hits in the other 35 units. This information, called hit pattern, is shared by all electronics boards through a "hit-pattern bus", which runs through the backplane. Besides the hit pattern information, other lines, such as power-lines and clock-lines also run through the backplane.

The signal flow from a well counter unit to a WPU board and a functional block diagram of the signal processing are shown in figure 11 and figure 12, respectively. There are two independent circuit blocks for the PMT and the PIN. Here we first describe the signal processing for the PMT and then for the PIN.
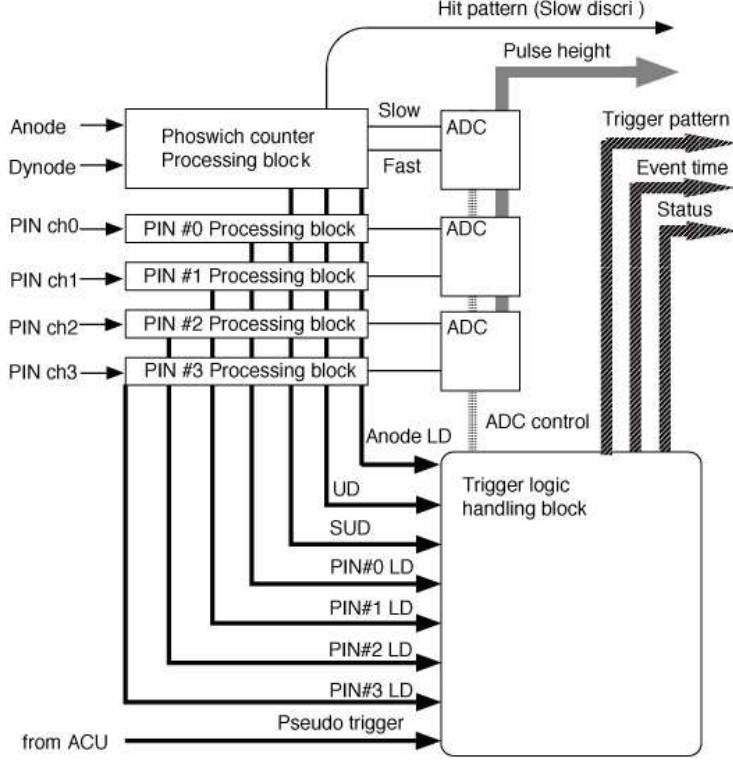
14

Fig. 12. Functional block diagram of the signal-processing part for a well counter.

The signal from a photomultiplier anode is fed directly to a fast amplifier in HXD-AE to generate trigger signals. Unlike the charge-sensitive amplifiers that are contained in the HXD-S front-end electronics and amplify dynode signals, the anode amplifier just simply amplifies the current from the photomultiplier. The power consumptions are 12.8 mW for the anode amplifier and 42.5 mW for the dynode amplifier. This allows us to utilize very short anode pulses, which are required in generating fast pre-trigger signals. This also has a special meaning in the present phoswich configuration: since the GSO scintillation has a faster decay time than that from BGO, valid GSO signals produce larger anode output pulse-heights than those from BGO, for the same energy deposit. This allows HXD-AE to preferentially select GSO signals, while rejecting BGO events.

A preamplifier output pulse generated from a dynode signal is split in the HXD-AE into two shaping chains with different time constants: 150 ns (fast shaping) and 1000 ns (slow shaping). Each of the shaped signal is then peak held (activated by the trigger signals) and sent to the analog to digital converters (ADCs). Since the decay times of the GSO and BGO are different, the ratio of the fast and slow shaping pulse heights will differ between GSO and BGO. In a fast-shaping processing chain, the charges from a BGO event are only partially integrated, while the GSO signal is fully integrated. In a slow-shaping processing chain, in contrast almost all the charges are integrated for both crystals. By comparing the fast and slow pulse heights, we can thus discriminate GSO pulses from BGO events. This "double integration method" is

15

the basis for pulse shape discrimination (PSD).

We have developed an Application Specific Integrated Circuit (ASIC) with this PSD function (Ezawa et al. 1996). When a dynode signal is fed to this ASIC and a trigger is received from the anode, the ASIC gives two peak-held analog outputs, corresponding to the two shaping time constants. The power consumption of the ASIC is 230 mW. These outputs can be arranged in figure 13, called "fast-slow diagram" or "two-dimensional spectrum", where the vertical and horizontal axes represent the slow and fast shaping pulse heights, respectively. In this way, we can see two lines with different inclination, or branches, demonstrating the separation of signals from GSO and BGO. A bridge connecting the two branches is formed by Compton-scattered events, which hit both GSO and BGO in the same unit, because their time constants are a mixture of the two. The actual selection is done by the ASIC in the WPU in the analog processing chain in each channel. We can compare the two pulse heights, either in HXD-AE, HXD-DE, or in ground analysis, to reject BGO events as well as Compton-scattered ones. Since the hardware threshold for the selection is rather loose, further selection is done by software in HXD-DE and in ground analysis.

While the PSD technique rejects the BGO signals in its own unit, the HXD has another important function to reduce background, called Hit Pattern Selection. This function utilizes hit pattern information from multiple units, and reject Compton scattered events that hit different units. Information on the hits of all 36 units (16 well units and 20 anti-counter units) is latched every time a valid event is acquired from any well counter unit. Although all information of 36 units can be used, the most dominant Compton scattering component in the energy range of ∼600 keV are those events scattered between the adjacent units. Since a Hit Pattern Selection using too many detector units will increase accidental coincidence and hence reduce the signal acceptance, it is generally adequate to consider the 4 adjacent units, or 8 surrounding units. The rejection pattern can be selected by software, either in HXD-DE, or in the course of ground analysis.

The signals from the four PINs inside the well-counter unit are separately read out and fed individually to low-noise charge-sensitive preamplifiers (PIN preamplifiers) mounted underneath the preamplifier for the PMT and fed into the circuit in HXD-AE. Analog electronics for the PIN is designed to achieve an energy threshold of 10 keV and an energy resolution of 3 keV (FWHM) in the orbit under power consumption of 107 mW for the preamplifier per each PIN diode. Since a PIN diode has a typical leakage current of ~ 2 nA at -20ºC, and relatively large capacitance of ∼50 pF (including the capacitance of the cable), we developed a low noise preamplifier with a capacitance gradient of ∼15 eV/pF. Since as many as 64 channels of PIN diodes need to be processed, reduction of the size and the power consumption is very important in the AE electronics. We therefore integrated the last step of the amplification, the peak-hold-circuit and the lower discriminator into the PIN as a variant to the PSD ASIC (Ozawa et al. 1997).
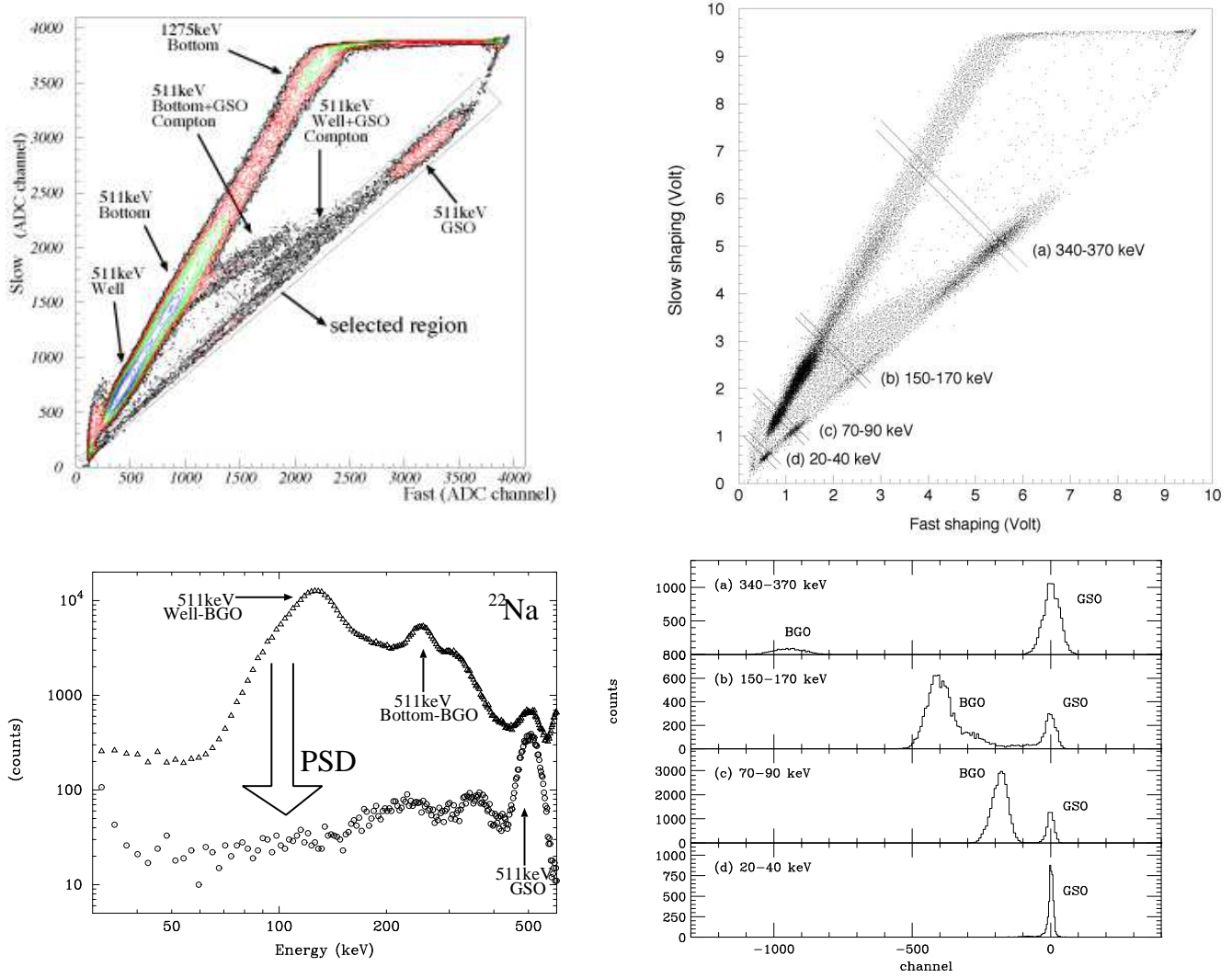
16

Fig. 13. (top) Fast-Slow diagram for the ^{22}Na and ^{133}Ba irradiation, taken from a single unit. (bottom-left) PSD selection effect on the GSO spectrum. (bottom-right) The separation of GSO/BGO events at the lower energy.

By combining the preamplifier with the PIN diode and operating them at -20°C, we achieved an energy resolution of 2.9 keV at 59.5 keV, and an energy threshold of ~ 10 keV, as shown in figure 14. The energy resolution of the PIN preamplifier is 1.0 keV in a load-free condition; this degrades to 1.6 keV by the capacitive noise, and another 1.0 keV is due to the current noise. The remaining ~ 2.1 keV is possibly caused by electronic noise in HXD-S or HXD-AE.

The trigger signal for the well-counter unit is generated from the anode signal, and for the PIN diodes, the output of the gain amplifier is fed into a comparator to generate the triggers. When any one of the trigger sources, including the pseudo trigger, is activated, gate signals for peak holding and ADCs are generated. The trigger rate in a single WPU could be as high as several hundred Hz, if we turn off the on board PSD selection. Therefore, careful design

17
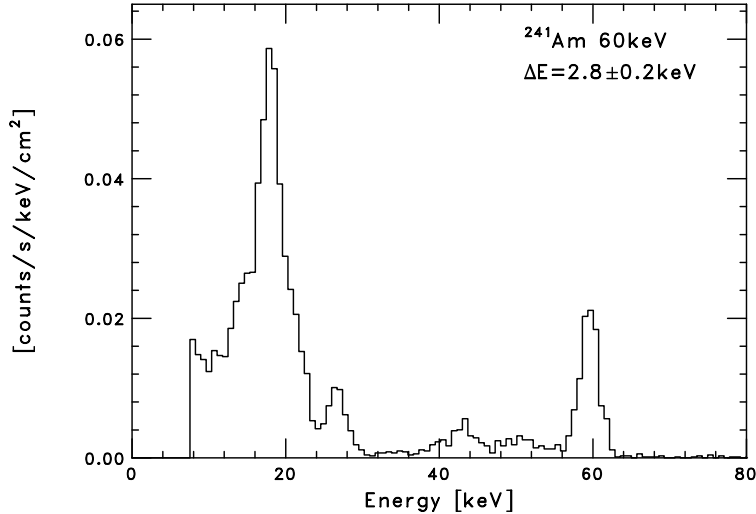
Fig. 14. PIN spectrum of ^{241}Am obtained at -20°C.

was adopted for the digital circuits that handle the triggering. By using the PSD information, the trigger is issued for events that deposited all of its energy in GSO or PIN. Signals with energies out of the energy range of the detector is also rejected based on the upper discriminator information. Hit-pattern information is used later in an offline analysis. The details of trigger sequence is described by Takahashi et al. (1998).

A significant fraction of these trigger events are charged particles, including geomagnetically trapped particles (mainly protons) and primary cosmic rays. Because the energy loss of a charged particle is proportional to the density and size of the detector, it becomes very severe in the HXD, which employs large and heavy scintillators for active shielding. In fact, the energy loss by a charged particle onto a HXD detector unit is estimated to be typically $\sim$100 MeV, which is 3 to 5 orders of magnitude larger than the target energy. Since this is well above the saturation level of the amplifying system, a long electronic recovery time would affect the subsequent signals, produce spurious events, and/or increase the dead time. In order avoid these problems and make the system tolerant to these large pulses with high counting rates, we have designed the whole electronics, from front-end to HXD-AE, to quickly recover from every energetic pulse. The recovery time for a 100 MeV pulse is about 50 μs for the dynode amplifier (Tanihata et al. 1999). Furthermore, we inhibit any subsequent trigger until the circuit has fully recovered from the disturbance caused by large pulses (Tanihata et al. 1999). The treatment for large pulses is also implemented in bleeder circuits in the photomultipliers for the well-counter units (Tanihata et al. 1999) and the anti-counter units. (Yamaoka et al. 2006)

The measuring the dead time is one of the most important tasks of the electronic system. This is because the spectrum of a celestial object is obtained by subtracting the back ground spectrum from the observed one, and an accurate live time is especially required when the source is faint. In the HXD, a dead-time measurement is done individually for each well unit

18

by counting the number of pseudo event pulse. The pseudo event pulses are electronic pulses generated in the ACU module, periodically with a selectable period. These pulses are fed into the trigger-handling block, and activates the trigger logic in the same way as other trigger sources, but with a specific flag in the trigger pattern. Since the pseudo trigger is randomly vetoed by normal events, we can accurately estimate the dead-time fraction, by comparing the total number of injected pseudo pulses and those actually recorded in the data. Another way to estimate the dead time is to count up to 10 MHz (selectable by command) by clock pulses when the system is busy, and hence the the trigger is inhibited. A verification of these methods in orbit is described in Paper II. The dead-time counters are edited into the monitor data and sent to HXD-DE every second. While the dead time counter cannot measure dead times caused by HXD-DE capability or by telemetry limitation, it can handle fast changes in the dead time.

The anti-counter units, which surround the 16 well-counter units, have two functions. One is to provide hit-pattern information to the well-counter units, and the other is to monitor celestial transient events, such as gamma-ray bursts and solar flares. Signals from each of the 5 anti-counter units on the same side of HXD-S are handled by one TPU module. In the TPU, hit-pattern signals from each counter are generated with an energy threshold of 40 keV. At the same time, a TPU module accumulates event pulses from the 5 anti-counter units, and produces their summed pulse-height spectrum, which is sent to HXD-DE every 1 s. If a sudden increase in the counting rate, due, e.g., to a gamma-ray burst, is detected, the TPU records four-energy-band light curves with a finer (15.625 ms or 31.25 ms) timing resolution for a certain length of time.

4.2. Data packet from HXD-AE

When an event from a well-counter unit satisfies the pre-specified trigger conditions and is hence judged to be valid, all analog outputs from the relevant Well unit (those of the slow shaper, the fast shaper, and the four diode shapers) are digitized by ADCs and edited into event data. For the signals of the PIN diodes, the upper 8 bits are used, because the dynamic range of the PIN diode is small (10 to 70 keV). Also recorded are the occurrences of any hits in four PIN diodes and GSO in the well unit as a trigger pattern. The pseudo trigger and the output from the discriminator that senses overshoot of the charge-sensitive amplifier of the PIN also provides trigger, which are recorded in the trigger pattern. Any hits in the slow discriminator output from 16 well units and 20 anti-counters are also recorded as a hit pattern. The output of the PSD, flags to monitor the pile-up events, and the upper discriminator outputs are also recorded. All arrival times are recorded with a resolution of 61μs during the normal operation mode. The data, formatted as shown in table 3, are sent to the HXD-DE on an event-by-event basis. Thus, one valid event occupies 18 Bytes. In addition to the well-event data, a number of additional data in the HXD system used to monitor its proper function and to estimate of the background and dead time are collected.

Table 3. WPU Envet Data

Channel ID	2 bit
Event Time	19 bit
Phoswich Counter Slow Pulse Height	12 bit
Phoswich Counter Fast Pulse Height	12 bit
PIN detector 0 Pulse Height	8 bit
PIN detector 1 Pulse Height	8 bit
PIN detector 2 Pulse Height	8 bit
PIN detector 3 Pulse Height	8 bit
Trigger Pattern	7 bit
PIN LD Trig	1 bit
Hit Pattern	36 bit
PSD Out	1 bit
PMT UD	1 bit
PIN UD	1 bit
PMT Double Trig Flag	1 bit
PIN Double Trig Flag	1 bit
Reset Flag	1 bit

4.3. Digital Electronics (HXD-DE)

HXD-DE is the CPU-based signal processing part of the HXD. It is designed: (1) to provide the primary interface with the satellite data processor for command and telemetry, (2) to control the acquisition and formatting of the data from HXD-AE, and (3) to react to events such as γ-ray bursts. HXD-DE is based on a CPU 80C386 running at 12 MHz. It has two CPU boards, with one board working while the other is idling for backup purposes. Mounted on the CPU board is 512 KB of SRAM used for a programmable area, another 512 KB of SRAM serving as direct memory access (DMA) buffer, and 512 KB of EEPROM for program storage.

One of the baseline requirements of HXD-DE is to acquire data without loss from sources that are several times as bright as the Crab Nebula. This means that HXD-DE should be capable of an acquisition rate of at least several hundred events per second. If we loosen the electronics parameters such as the level of PSD discrimination and low-level discriminator, the rate goes up quickly. Therefore we set our rate tolerance of system to be 4,000 events per second. In order to achieve this high acquisition rate with limited hardware resources, we use a fast real time operating system specially designed for this experiment, in conjunction with a circuit capable of receiving data from HXD-AE by the DMA mode. When data are sent or received in the DMA mode, the I/O adaptor accesses the DMA buffer directly, without interrupting the CPU.

In orbit, irradiation by charged particles can cause bit errors in the memory. In order to prevent these errors from causing malfunctioning, the process called Memory-Patrol is always running to verify the contents of memory byte by byte. In addition, the HXD-DE data are accompanied by an error correction code, which repairs 1-bit errors, and reports the occurrence of 2-bit (or more) errors.

4.4. PI PROGRAM

The process called "PI program" is an important addition to the HXD-DE software, and is used to realize high signal throughput while keeping a low background capability. Its task, for example, is to filter out those background events that leak through the hardware selection in WPU, and to compress the "transient" data sent from the TPU. These functions becomes particularly important when the telemetry bandwidth is limited. Additional tasks of the PI program are to collect calibration data, and to notify γ-ray burst triggers to the TPU modules. The PI program is activated when the data arrives from the DMA buffer with the data type as input. According to the data type, the main routine of the PI program calls the corresponding function that handles the data.

Although the hardware PSD in the WPU module is very powerful, the PI program provides more flexible ways to further select events. The PI program does the event selection via several different algorithms, which can be chosen by commands. Several examples of these algorithms are given below:

hit pattern: The program performs event selection based on the hit pattern information of the surrounding units. Using this, we can reject Compton scattered events and particle-interaction events.

pulse shape: In HXD-AE, pulse-shape discrimination is performed by comparing the pulse heights between the slow and fast shaping amplifier outputs. In HXD-DE, finer and more flexible selections can be applied on the fast-slow diagram.

delta-t: In some inorganic scintillators, such as CsI(Tl), a train of pulses with random shapes occur during 400 μs - a few ms after a large energy deposit (at least E$\geq$ 60 MeV) in the crystal (Takahashi et al. 1993). This leads to a number of false triggers in a very short time. These false events can be removed in the HXD-DE, because the PI program can measure the time difference between successive events and remove them if the difference is shorter than a certain threshold.

5. Ground Calibration and Tests

Before the launch, the HXD performance was studied extensively on the ground. Since the HXD is a highly sophisticated experiment involving a large number of components, a comprehensive data base has to be prepared before launch in order to construct a set of software required to deduce scientific results from the observational data. In ground pre-launch tests, we
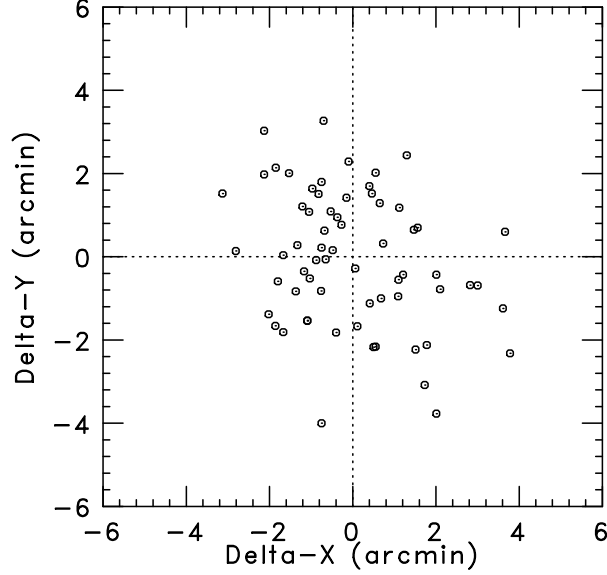
Fig. 15. Pointing offsets of the fine collimators in X- and Y- directions measured by scanning a radio active source in front of HXD-S.

first qualified the basic system functions, including the pulse shape discrimination, hit pattern generation, and the methods of dead time measurements. Subsequently, we placed HXD-S in a low-temperature environment ($-20°$C), irradiated it with various gamma-ray emitting radio isotopes, and acquired data via HXD-AE and HXD-DE. We thus measured the basic characteristics of individual well-counter and anti-counter units, including the gain linearity and energy resolution, as well as their angular responses. The background spectrum was also measured to verify the low background performance of the HXD.

5.1. Alignment

The alignment of the 64 fine collimators has been measured by means of optical laser light and a γ-ray source. Figure 15 shows their angular offsets measured by scanning a ^{133}Ba source in front of HXD-S at some distances. These two independent measurements confirm that the collimators are aligned with an accuracy of 3.5′ (FWHM). This ensures an effective transparency of 90%, when a target is placed at the mean direction of the optical axes of the 64 fine collimators. We verify that the angular offsets did not change after the vibration test of HXD-S. The effective area shown in figure 9 has to be collected with this effective transparency. The overall calibration for the absolute normalization in orbit is described in Paper II.

5.2. Spectral performance

Calibrations of gains and offsets and measurements of energy resolution are essential in constructing the instrumental response function, which in turn is needed to reconstruct incident spectra from the observed pulse-height distributions. Before assembling HXD-AE, we measured the linearity and dynamic range of its individual signal-processing circuits using electronic test

22

pulses. After some iterative electronics gain and offset adjustments, the relations between the test pulse amplitude and the resultant ADC values of individual signal channels were measured, and were registered as gain parameters in a calibration data base.

When mono-energetic gamma-rays are incident on the PIN or GSO detector, the output pulse height distribution primarily consists of a roughly Gaussian peak formed by full-energy-deposit events. Although the Gaussian centroid is roughly proportional to the gamma-ray energy, we must consider the measured electronics non-linearity (see above). Furthermore, GSO scintillator is known to exhibit some non-linearity between its energy deposit and light output, particularly toward lower energies (Uchiyama et al. 2001); this has to be calibrated. The pulse-height distributions also very often show secondary features with lower pulse heights. In the GSO spectra, the strongest secondary feature is produced by gamma-rays that undergo Compton scattering in the detector and escape from it. In the PIN spectra, guard-ring structures in the diode produce a spectral sub-peak with a $\sim 2/3$ of the main-peak pulse height (Sugiho et al. 2001). Since these secondary features generally depend on the detector geometry, we use Monte Carlo simulation code, either EGS4 (Nelson et al. 1985) or Geant4 (Allison et al. 2006; Agostinelli et al. 2003), to compute the response of the HXD detector as a continuous function of energy (Terada et al. 2005; Kokubun et al. 2006). These codes allow us to handle the detailed detector geometry, such as the guard ring and housing of the PIN diodes. These Monte Carlo simulations refer to the data base, which summarizes parameters of individual GSO and PIN detectors such as the linearity and the energy resolution, measured at discrete energies using isotopes by fitting the spectrum with a Gaussian profile. Sub peak structures seen in the PIN spectrum are properly taken into account in the code.

After HXD-S and HXD-AE were assembled, we measured the linearity and energy resolution, including both the sensor and electronics properties, utilizing gamma-ray lines from radio isotopes listed in Table 4. The obtained PIN and GSO spectra are shown in figure 16 and figure 17, respectively. The GSO spectrum clearly reveals the 31 keV Kα line from ^{133}Ba, indicating that the lower threshold energy of GSO has been made sufficiently low. The phoswich configuration successfully prevents the Compton events from contaminating the GSO spectra, and makes the full-energy peaks much more prominent than in the spectra taken with conventional scintillators. Figure 18 and figure 19 shows linearity plot of one representative PIN and GSO, respectively, obtained from these γ-ray line measurements. Below ~ 100 keV, the GSO results show the slight non-linearity mentioned above, which can be corrected by the analysis software.

As can be inferred from figure 16, and summarized in figure 20, the typical energy resolution of the PIN diodes has been obtained as ~ 3.3 keV at -20°C. This meets our design goal, because then the low-energy threshold of PIN can be lowered to ~ 10 keV, ensuring an overlap with the energy range of the XIS (Koyama et al. 2006). Similarly, figure 21 shows the distribution of energy resolution of the GSO scintillator in the 16 well-counter units, while
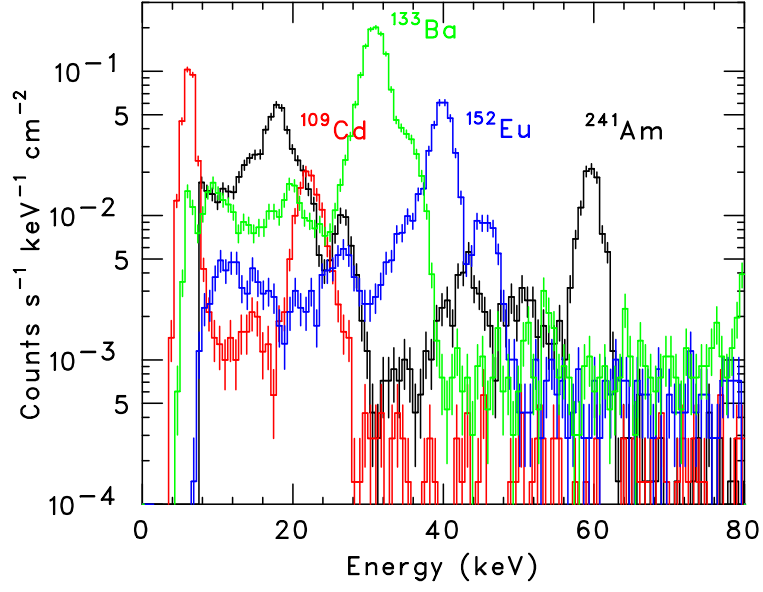
Fig. 16. Composite energy spectra of the PIN diode, from various γ-ray isotopes, are superposed for presentation (W01 for ^{241}Am, W12 for ^{109}Cd, W23 for ^{152}Eu, and W33 for ^{133}Ba.
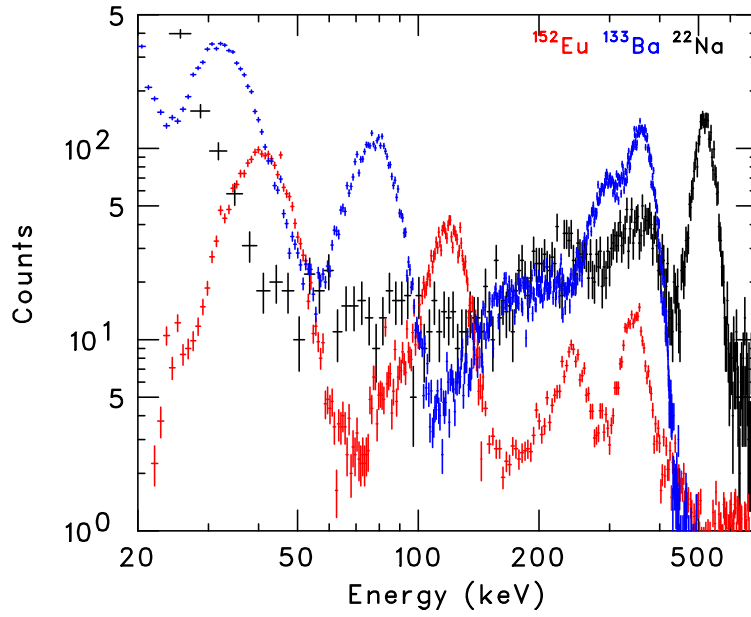

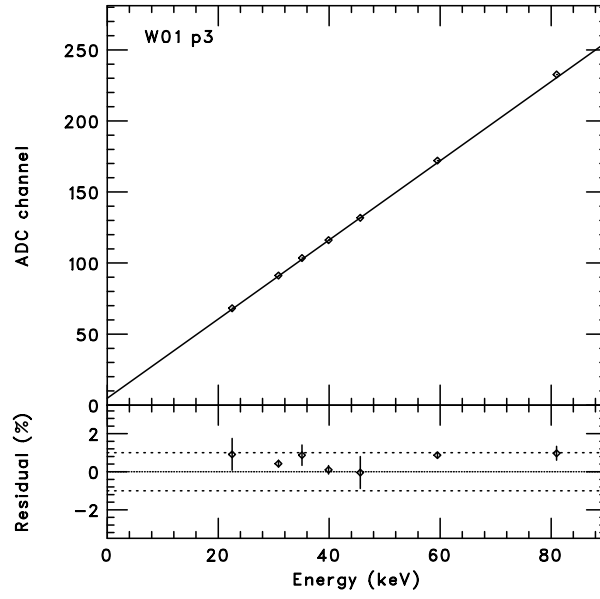**Fig. 17.** The same as figure 16, but for GSO.

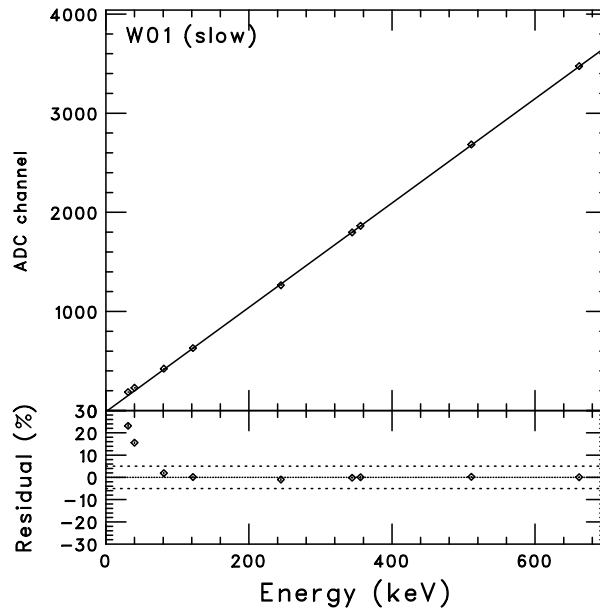**Fig. 18.** Pulse-height vs energy linearity of the well-counter unit W01 (PIN03).

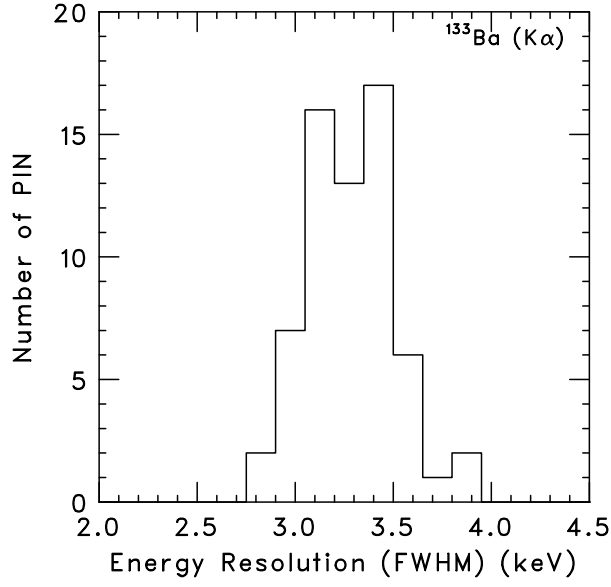**Fig. 19.** The same as figure 18, but for GSO in the well-counter unit W01.

Fig. 20. Distribution of the energy resolution among the 64 PIN diodes in the HXD, measured at -20°C using the 31.5 keV γ-ray line from ^{133}Ba .
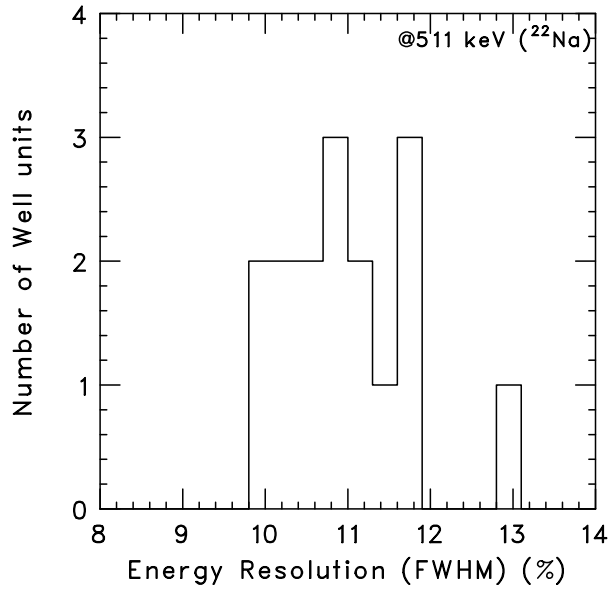
Fig. 21. Distribution of the energy resolution of GSO in the 16 well-counter units, measured using the 511 keV γ-ray line from ^{22}Na.
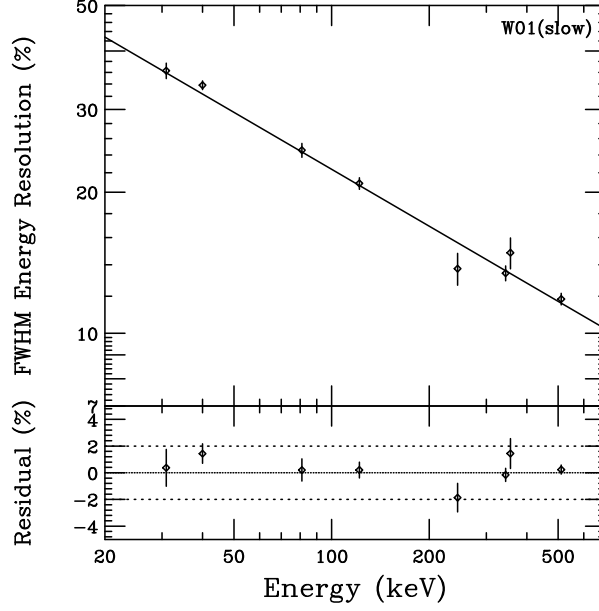
Fig. 22. Energy dependence of the GSO energy resolution measured with the unit W01.

figure 22 shows the energy resolution of unit W01 as a function of energy. Thus, the energy resolution is 12% at 511 keV (or 10% at 662 keV), which again meets our design goal. The corresponding value of a single GSO of 5 mm thick read directly by a PMT is typically 7% at 662 keV, and its degradation to $\sim 10\%$ is caused by the phoswich configuration: about 30% of the GSO scintillation photons are absorbed when they penetrate the BGO bottom piece, and another $\sim 20\%$ is reflected into the BGO top piece.

Table 4. Radio isotopes used for the calibration of the PIN and the GSO detectors in the Well-counter units.

Isotope	Energy (keV)	
^{109}Cd	22	PIN
^{133}Ba	31.5	PIN
^{152}Eu	41.1	PIN / GSO
^{241}Am	59.5	PIN / GSO
^{133}Ba	81	GSO
^{152}Eu	122	GSO
^{152}Eu	344	GSO
^{22}Na	511	GSO

5.3. *Background level and expected sensitivity*

It is of vital importance to confirm that the HXD achieves a sufficiently low background level, after the event selections implemented in the HXD are applied. Figure 23(a) shows a

27

ground background spectrum of a typical well-counter unit, acquired in these pre-launch tests. It is presented in the same fast-slow diagram as figure 13. Again, we clearly observe the separation of the GSO and BGO branches. Below the GSO branch, we can see a narrow line. Because of the very fast time constant attributed to these events, they are thought to be due to Cherenkov light produced in PMT glass. Figure 23(b) shows the events selected by the PSD in the data analysis; the selection here is somewhat tighter than is implemented in HXD-AE as hard-wired function (subsection 4.1), but comparable to those that will be employed in actual observations. It is apparent that all of the BGO and Compton events are effectively rejected by the PSD cut. Further details on the selection criteria in the fast-slow plane are described in Tanihata et al. (1998) and Paper II.

Figure 24 is the PIN and GSO background spectra thus obtained on ground after the PSD selection; the latter spectrum is equivalent to the horizontal projection of the 2-dimensional spectrum in figure 23(b). Thus, the PIN background spectrum is rather featureless except Gd K lines from the GSO scintillators seen at ~ 45 keV, while that of GSO exhibits a prominent peak around 360 keV. At this stage, the measured on-ground background level thus becomes $\lesssim 1 \times 10^{-4}$ cnts s^{-1} cm^{-2} keV^{-1} over the entire HXD energy range, 10–600 keV.

The remaining background events are further reduced by taking anti coincidences among the 16 well-counter and 20 anti-counter units, employing the hit pattern information attached to individual GSO events (subsection 4.2). The solid line in figure 24 shows the background spectrum after hit pattern selection by adjacent 4 units for both GSO and the PIN diodes. For the PIN diodes, the events that hit the BGO or GSO in its own well unit are also rejected. The effect of anti-coincidence among units by utilizing hit pattern information reduces the background level by 30–50 %. In the GSO selected spectrum (figure 24), it is apparent that while the background level under 100 keV is determined by off-aperture X-rays from the FOV, it is dominated by the intrinsic radio activation above 100 keV. A peak around 360 keV is clearly seen. This is due to the intrinsic radioactivity of the ^{152}Gd in the GSO crystal (abundance 0.2%, 2.14 MeV α-ray, half-life 1.1×10^{14} year) (Kamae et al. 1993). The number of photons of the peak is counted to be 0.2 cts/s per well, which is consistent with the calculated value. Though this intrinsic peak cannot be removed, we utilize it as an in-orbit calibration source, while we use activation lines of GSO and BGO for PIN (Paper II). The resulting background level at the sea level was $\sim 1 \times 10^{-5}$ cts s^{-1} cm^{-2} keV^{-1} at 30keV for the PIN diodes, and $\sim 2 \times 10^{-5}$ cts s^{-1} cm^{-2} keV^{-1} at 100 keV, and $\sim 7 \times 10^{-6}$ cts s^{-1} cm^{-2} keV^{-1} at 200 keV for the phoswich counter. This is the lowest background level we have reached throughout our development, including the balloon experiments (Takahashi et al. 1993).

In orbit, the background level is expected to increase because charged particles penetrating through the scintillators will produce various unstable nuclear isotopes. We have thus carried out proton irradiation experiments using particle accelerator facilities, in which a flight-equivalent well and anti units were both irradiated by protons accelerated up to typical energies
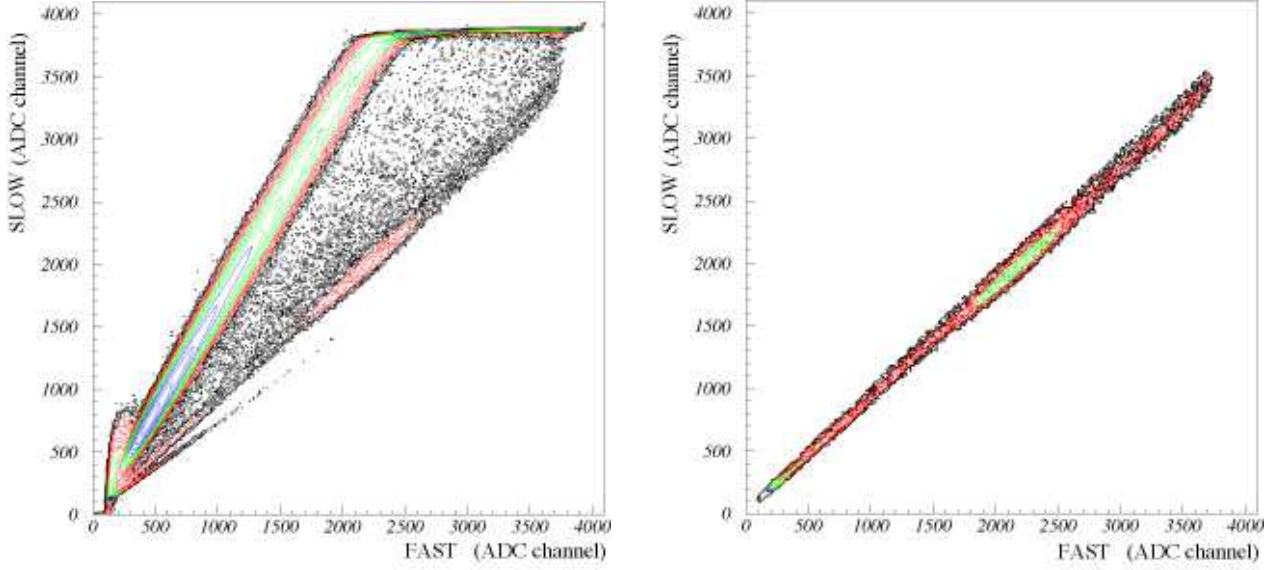
Fig. 23. Background spectrum of a typical well-counter unit measured on the ground, presented on a fast-slow plane. (a) Total background events detected by the phoswich counter. (b) Events selected by the PSD (see text) , both taken from a single unit

(100–200 MeV) of the geomagnetically trapped cosmic-rays in orbit. Figure 25 represents the expected background spectrum in orbit, obtained by adding together the measured on-ground background and the expected increase due to radio-activation. The latter was calculated assuming a proton flux in an orbit of altitude of 550 km and inclination of 31 °at the solar maximum. (Kokubun et al. 1999).

The sensitivity of a detector for a weak continuum source is generally determined by statistical and systematic uncertainties in the background, the effective area in the relevant energy range, and the observation time. The very low background level demonstrated by the ground calibration ensures a high sensitivity for the HXD, even with its relatively small effective area. The expected sensitivity will be presented in the companion paper (Paper II), taking into account the actually measured in-orbit background and its variation.

In order to achieve a high sensitivity, precise modeling of the background is important. For this purpose, we turn on the PIN diodes even in the SAA passage to count the number of energetic charged particles that have passed through PIN diodes. By utilizing the count rate of upper discriminators attached to each analog processing chain for the PIN diode, the information about the nature of non X-ray background can be obtained by measuring a variation and distribution of such high energy particles. Detail results of measurements and their application to the modeling are described in Paper II.
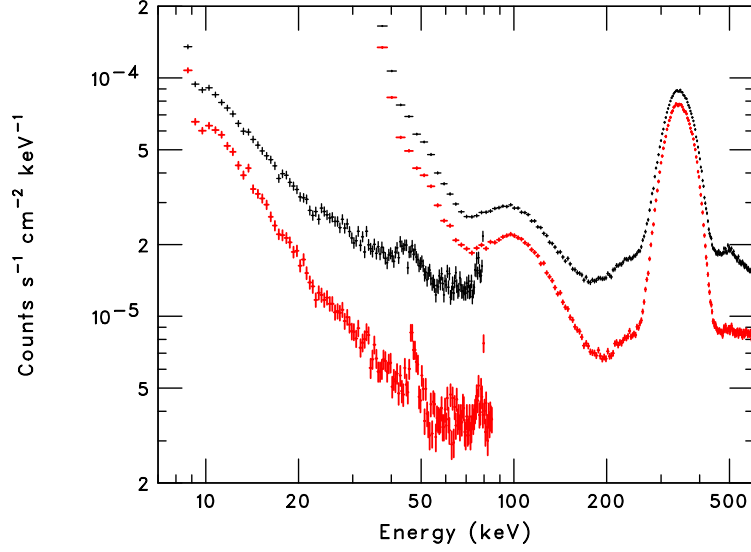
29

Fig. 24. Background spectrum obtained from a ground calibration. The black line represents the spectrum selected by PSD, and the red line represents the spectrum additionally selected using the hit pattern from 4 adjacent units for rejection.
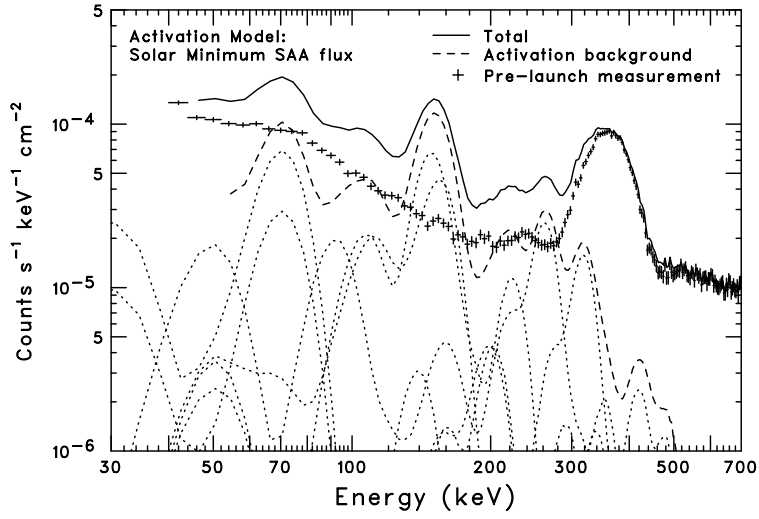

Fig. 25. Expected in-orbit GSO background spectrum at energies above 40 keV (solid line). It is based on the measured on-ground background (crosses), and includes estimated activation backgrounds (dashed line) calculated from our beam experiment (Kokubun et al. 1999). The dotted lines show individual activation components.

6. Summary

The HXD has been designed to achieve an extremely low in-orbit background ($\sim 10^{-4}$ c s^{-1} cm^{-2} keV^{-1}), based on a combination of novel techniques: (1) five-sided tight BGO active shielding; (2) the use of the 20 shielding counters made of thick BGO crystals that surround the 16 main GSO/BGO counters; (3) sophisticated onboard signal processing and onboard event selection, employing both high-speed parallel hardware circuits in the Analog Electronics, and CPU-based signal handling in the Digital Electronics; and (4) a careful choice of materials that do not become strongly radio-activated under in-orbit particle bombardment. Finally, (5) the narrow field of view below ~ 100 keV, defined by the fine collimator, effectively reduces both the CXB contribution and any source confusion. A detailed pre-flight calibration confirms that the performance of the HXD meets the design goal of the experiment, including the threshold of ~ 10 keV of the PIN diode, and the very low on-ground background of $1 - 5 \times 10^{-5}$ counts sec^{-1} keV^{-1} cm^{-2}.

References

Agostinelli, S. *et al.*, 2003, NIM-A, 506, 250

Allison, J. *et al.*, 2006, *IEEE Trans. Nucl. Sci.*, 53, 270

Band D., et al.1993, ApJ, 413, 281

Ezawa H., et al.1996, IEEE Trans. Nucl. Sci., 43, 1521

Fishman, G. J., et al.1989, in Proc. GRO Science Workshop, ed. W. N. Johnson (Greenbelt: NASA/GSFC), 2-39

Fukazawa Y. et al.2006, Proc. SPIE, 6266, in press

Hayashida, K., et al., 1989, PASJ, 41, 373

Kamae T., et al.1993, IEEE Trans. Nucl. Sci., 40, 204

Kamae T., et al.1992, Proc. SPIE, 1734, 2

Kamae T., et al.1996, Proc. SPIE, 2806, 314

Kamae T., et al.2002, Nucl. Instr. Meth. A490 456

Kawaharada M., et al.2004, Proc. SPIE, 5501, 286

Kokubun M., et al.1999, IEEE Trans. Nucl. Sci., 46, 371

Kokubun M., et al.2004, IEEE Trans. Nucl. Sci., 51, 1999

Kokubun, M.et al. 2006, PASJ, in press,

Koyama, K. et al. 2006, PASJ, in press,

Mitsuda, K. et al. 2006, PASJ, in press,

Nakazawa K., et al.1999, Proc. SPIE 3765, 148

Nelson W. R., Hirayama H, Rogers D. W. O., 1985, SLAC-Report-265

Ota N., et al.1999, Nuclear Instruments and Methods in Physics Research A436, 291

Ozawa H., et al.1997, Proc. SPIE 3115, 235

Sugiho M., et al.2001, IEEE Trans. Nucl. Sci. 48, 426

Takahashi T., et al.1993, IEEE Trans. Nucl. Sci. 40, 890

Takahashi T., et al.1998, Proc. SPIE 3445, 155

Tanihata C., et al.1999, Proc. SPIE 3765, 645

Tashiro M., et al.2002, IEEE Trans. Nucl. Sci. 49, 1893

Terada Y., et al.2005, IEEE Trans. Nucl. Sci. 52, 902

Uchiyama Y., et al.2001, IEEE Trans. Nucl. Sci. 48, 379

Yamaoka K. et al.2006, Proc. SPIE 6266, in press

Present Address

* Fujitsu System Solutions Ltd., Bunkyo Green Court Center Office, 2-28-8 Honkomagome, Bunkyo-ku, 113-0021

† Mitsubishi Electric Company,325 Kamimachiya, Kamakura,247-8520

‡ Nihon University, 7-24-1, Narashinodai, Funabashi, 274-8501

§ Goldman Sachs, Japan Ltd. 6-10-1, Roppongi, Minato-ku, 101-6144

¶ NASA/Goddard Space Flight Center, Greenbelt, MD 20771, USA.

∥ Ministry of Economy, Trade, and Industry, Kasumigaseki, Chiyoda, 100-8917

** Tokyo Institute of Technology, 2-12-1 Ookayama, Meguro, 152-8551

††Japan Patent Office, Kasumigaseki, Chiyoda, 100-8915

‡‡ deceased

§§ Tecnets Co., 3-3-5 Owa, Suwa, 392-8502

¶¶ Agilent Technologies Japan, Ltd., 9-1 Takakura-cho, Hachioji, 192-8510

∥ NEC-Toshiba Sapce Systems, Ltd., 1-10 Nissin, Fuchu,183-8551

*** ITFOR Inc, 21 Ichibancho, Chiyoda-ku, 102-0082

††† Hitachi Ltd., 7-1-1 Omika-machi, Hitachi, 319-1292